

DASPy: A Python Toolbox for DAS Seismology

Minzhe Hu¹ and Zefeng Li^{1, 2*}

1. *Laboratory of Seismology and Physics of Earth's Interior, School of Earth and Space Sciences, University of Science and Technology of China, Hefei, China*

2. *Mengcheng National Geophysical Observatory, University of Science and Technology of China, Mengcheng, China*

Corresponding author: Zefeng Li (zefengli@ustc.edu.cn)

Manuscript submitted to *Seismological Research Letters*

June 20th, 2024

Abstract

Distributed acoustic sensing (DAS) has emerged as a novel technology in geophysics, owing to its high sensing density, cost-effectiveness, and adaptability to extreme environments. Nonetheless, DAS differs from traditional seismic acquisition technologies in many aspects: big data volume, equidistant sensing, measurement of axial strain (strain rate), and noise characteristics. These differences make DAS data processing challenging for new hands. To lower the bar of DAS data processing, we develop an open-source Python toolbox called DASPy, which encompasses classic seismic data processing techniques, including preprocessing, filter, spectrum analysis, and visualization, and specialized algorithms for DAS applications, including denoising, waveform decomposition, channel attribute analysis, and strain-velocity conversion. Using openly available DAS data as examples, this paper makes an overview and tutorial on the eight modules in DASPy to illustrate the algorithms and practical applications. We anticipate DASPy to provide convenience for researchers unfamiliar with DAS data and help facilitate the rapid growth of DAS seismology.

1 Introduction

Distributed acoustic sensing (DAS) is an emerging vibration monitoring technology increasingly utilized in geophysics. It converts fiber optic cables into an ultradense seismic array with meter-scale spacing and a frequency range of 0.01 Hz to 100 kHz. DAS recovers axial strain or strain rate along the fiber-optic cable by measuring the subtle optical phase shift of backscattered light within the fiber (Lindsey & Martin, 2021; Zhan, 2019). Over recent years, it has been demonstrated useful in many seismological applications such as earthquake monitoring (Z. Li et al., 2021; Z. Li & Zhan, 2018; Lindsey et al., 2017; Nayak et al., 2021; Zeng et al., 2022), source property estimate (Chen, 2023; J. Li, Kim, et al., 2023; J. Li, Zhu, et al., 2023), subsurface imaging (Ajo-Franklin et al., 2019; Cheng et al., 2021; Dou et al., 2017; Luo et al., 2021; Nayak & Ajo-Franklin, 2021; Yang, Atterholt, et al., 2022), fault zone detection (Atterholt, Zhan, & Yang, 2022; Jousset et al., 2018; Lindsey et al., 2019; Yang, Zhan, et al., 2022) and urban seismology (Lindsey, Yuan, et al., 2020; X. Wang et al., 2021; T. Zhu et al., 2021). It has also been applied broadly outside seismology, such as volcanology (Jousset et al., 2022; Nishimura et al., 2021), oceanography (Lin et al., 2024; Sladen et al., 2019; Williams et al., 2019, 2022; Xiao et al., 2022), glaciology (Hudson et al., 2021; Walter et al., 2020), marine biology (Bouffaut et al., 2022; Landrø et al., 2022; Rørstadbotnen et al., 2023; Wilcock et al., 2023), and meteorology (Hong et al., 2024; T. Zhu & Stensrud, 2019).

DAS produces data gathers with regular spacing, similar to exploration seismic data. Hence, one may process DAS data with software for exploration data, such as Seismic Unix (Cohen & Stockwell, 2008) and Madagascar (<http://www.reproducibility.org>). However, compared to conventional seismic arrays in earthquake seismology, DAS differs in several key aspects, especially the voluminous data and uniaxial measurement of strain or strain rate (Z. Li, 2021; Lindsey & Martin, 2021; Zhan, 2019). The noise composition of DAS tends to be more complex due to its different self-noise, common-mode noise, and traffic noise for often along-road fibers (Bakku, 2015; Costa et al., 2019; Lindsey, Rademacher, et al., 2020; Zhirnov et al., 2019). These differences often require different processing techniques from those for conventional seismometers, making it challenging for researchers newly using DAS data.

Inspired by the success of ObsPy for conventional seismic data processing (Beyreuther et al., 2010), we believe that a new Python processing package specifically designed for DAS data could facilitate the development of DAS seismology. We notice that an ongoing project, called DASCORE, is developing a Python package for reading and writing, visualization, and basic processing of DAS data (Chambers et al., 2024). In this study, in addition to the functionalities offered by DASCORE, we aim to provide a wider diversity of practical data processing tools dedicated for DAS applications. This new open-source Python package is named DASP and comprises two primary components: a set of basic tools including modules for preprocessing, filtering,

frequency attributes and visualization, and another set of advanced tools including modules for channel analysis, waveform decomposition, denoising and strain-velocity conversion (Fig. 1). As follows, we showcase the key functionalities using various publicly available datasets (Fig. 2) and ensure that the experiments can be easily replicated by readers.

2 Basic Tools

2.1 Classic processing techniques

Typical seismic data processing includes filtering, frequency attribute analysis and certain preprocessing methods. We wrap these techniques for 2-dimensional DAS data, eliminating the need for iterating over channels. For example, the Python code below bandpass filters the data from the RAPID dataset (Wilcock & Ocean Observatories Initiative., 2023; <http://piweb.ooirsn.uw.edu/das/>; Figure 2a) between 15 and 27 Hz and yields a spectrogram averaged over 100 channels and a frequency-wavenumber (FK) spectrum (Figure 3). This dataset was collected offshore central Oregon and recorded various signals including fin whale calls, northeast Pacific blue whale A and B calls, and ship noises (Wilcock et al., 2023).

```
>>> from daspy.basic_tools.filter import bandpass
>>> from daspy.basic_tools.freqattributes import spectrogram, fk_transform
>>>
>>> data_filtered = bandpass(data, fs, 15, 27, detrend=True, taper=0.04)
>>> spec, f1, t = spectrogram(data[4880-50:4880+50], fs=fs, nperseg=256, noverlap=246,
                             nfft=1024, detrend=True)
>>> fk, f2, k = fk_transform(data, dx, fs)
```

92

93 2.2 Visualization

94 The function, `plot`, can be used to visualize 2-dimensional DAS data. It offers a
95 number of optional parameters to accommodate the users' requirements for plotting a
96 variety of data types, such as waveforms, spectra, spectrograms, and FK spectra. Below
97 is the Python code for visualizing the data in the previous example: unfiltered and
98 filtered data, the spectrogram and the FK spectrum (Figure 3). The bandpass filtered
99 waveform reveals high-frequency fin whale calls, with amplitudes approximately four
100 to five orders of magnitude lower than the ocean wave signals (Figure 3b). The
101 spectrogram demonstrates the sequential production of high- and low-frequency calls
102 by the fin whale (Figure 3c). The FK spectrum reveals an apparent velocity of this
103 acoustic signal exceeding 1400 m/s along the axial direction of the optical cable (Figure
104 3d).

105

```
>>> from daspy.basic_tools.visualization import plot
>>>
>>> fig, ax = plt.subplots(4, 1, figsize=(7,8))
>>> plot(data, dx=dx, fs=fs, ax=ax[0], transpose=True, x0=xmin*dx, xlabel=False,
        colorbar_label='Strain')
>>> plot(data_filtered, dx=dx, fs=fs, ax=ax[1], transpose=True, x0=xmin*dx,
        xlabel=False, colorbar_label='Strain')
>>> plot(Zxx, fs=fs, obj='spectrogram', ax=ax[2], f=f1, t=t, vmin=2e-8, vmax=3e-6,
        ylim=[0, 40])
>>> plot(fk, obj='fk', ax=ax[3], f=f2, k=k, xlim=[-0.025, 0.025], ylim=[0, 40],
        vmin=0.05, vmax=0.2)
>>> plt.tight_layout(pad=0.5)
>>> plt.savefig('figure3.pdf', dpi=1200)
```

106

107

3 Advanced Tools

3.1 Channel analysis

DAS channels have equidistant spacing but the location of each channel is often unknown and requires tap tests. Besides, the linearity and ground coupling of the fibers often need to be taken care of. We develop three functions for channel location and quality analysis: channel location interpolation, turning point detection, and low-quality channel checking.

Channel location interpolation for DAS is calculated using two types of inputs: points with known channel numbers, and optional fiber spatial track points without channel numbers. Points with known channel numbers are typically acquired through tap tests and are often sparse. The spatial fiber track points are used to constrain the array geometry. They are optional but dense track points are particularly useful for accurate location interpolation. Fig. 2a shows examples of the two DAS arrays of the RAPID dataset (Wilcock & Ocean Observatories Initiative., 2023). In DASPy, we implemented the interpolation method used by the RAPID team, in which interpolation is performed after the coordinates are projected to the Universal Transverse Mercator (UTM) coordinate system.

The turning point detection function determines the points where the fiber strike varies noticeably based on the given channel coordinates or based on waveform coherency

across neighboring channels. The application of the coordinate-based detection function to Brady's geothermal field DAS array (University of Wisconsin, 2016a; <https://gdr.openet.org/submissions/829>; Fig. 2c) produces results consistent with those of Piana Agostinetti et al. (2022). As cross-channel waveform coherency is not only affected by the fiber strike angle, but also controlled by other factors including the quality of the backscattered light, coupling conditions and small-scale scatterers at different locations, its results could be less stable than those of coordinate-based computations assuming the coordinates are accurate. However, when the coordinates are unavailable or inaccurate, inference from cross-channel waveform coherency could be an alternative.

The channel quality checking function detects segments with obvious poor coupling (e.g., zip-tied loops of telecommunication cables) by identifying outliers of waveform energy along the fiber. It fits the waveform energy (the square of the amplitudes) variations with channels by a high-order polynomial and removes the fitted polynomial from the data. A threshold of four times of standard deviation below the median is set to identify the outliers. We assume that poor coupling tends to be spatially continuous. Hence, isolated normal values among a group of outliers would be identified as bad channels and vice versa. Using this function, we assess the channel quality of Ridgecrest DAS (Fig. 2d) with 15 seconds of traffic noise (Atterholt, 2021; <https://data.caltech.edu/records/1955>, Fig. 4). Our waveform-based detection results

are generally consistent with the hand-picked results of Atterholt, Zhan, Shen, et al. (2022) (Fig. 4b-f), except for the initial segment which was identified from a priori knowledge during field installation. It is noteworthy that the spikes (Fig. 4a) do not significantly influence the low-quality channel detection because we use a robust fit for the waveform energy (abnormal points are excluded from fitting).

3.2 Data denoising

As aforementioned, DAS data are often mixed with complex types of noise. DASPy integrates functions for the removal of typical noise types, including spike noise (Bakku, 2015), common-mode noise (Lindsey, Rademacher, et al., 2020), stochastic noise (Costa et al., 2019), and coherent noise. DASPy constructs a denoising module that incorporates three methods that take advantage of different noise properties.

Spikes are unusually large amplitudes (Fig. 5a) and could be caused by laser frequency drift or laser noise (Zhirnov et al., 2019). The spike removal function first applies the across-channel median filter and then the across-time median filter to generate a median map from the absolute amplitudes. Points with amplitudes exceeding a predefined threshold of the median map are identified as spikes. All spikes are subsequently substituted with interpolated values from adjacent channels. The spike removal function is validated using an earthquake waveform recorded by the Stanford-I DAS array (Fig. 2b and Fig. 5a-b; Biondi et al., 2017; Martin et al., 2017).

171

172 Common-mode noise, also known as in-phase noise is generated by vibrations of the
173 optoelectronic system and arises on all channels simultaneously (Fig. 5d). DASP
174 employs spatial averaging of waveforms to obtain common mode noise. Subsequently,
175 we compute the correlation coefficient with the channel record and the common-mode
176 noise, multiply the common-mode noise by the coefficient, and subtract it from the
177 channel record. We evaluate the common-mode noise removal algorithm using a
178 segment of offshore channels of the RAPID dataset (Wilcock & Ocean Observatories
179 Initiative, 2023; Fig. 2a). The processing effectively mitigates the common-mode noise
180 (Fig. 5d-e).

181

182 The inherent stochastic noise in DAS data is primarily caused by instrumental
183 deficiencies such as sampling error and phase noise (Costa et al., 2019). The fast
184 discrete curvelet transform (FDCT) (E. Candès et al., 2006; E. J. Candès & Donoho,
185 2004) is used to obtain an effective non-adaptive sparse representation of the regular-
186 spaced DAS seismic data and remove stochastic noise (Atterholt, Zhan, Shen, et al.,
187 2022). The basis functions of curvelet transform are defined as polar wedges in the FK
188 domain and represent the object position, scale, and angle. The curvelet denoising
189 function uses a silent DAS recording to estimate stochastic noise. After FDCT, the
190 amplitude of the curvelet coefficients is used as an empirical threshold. By default,
191 DASP employs a soft threshold to remove stochastic noise in the curvelet domain. We

192 apply curvelet denoising to the spike-removed waveform of Stanford-1 DAS (Biondi
193 et al., 2017; Martin et al., 2017; Fig. 2b and Fig. 5b), resulting in a notable reduction in
194 stochastic noise before the arrival of P waves (Fig. 5c).

195
196 Coherent noise can be defined as any coherent signal that are not of interest. For
197 example, for studies on an earthquake, a traffic signal is coherent noise; for studies on
198 traffic footprints, an earthquake signal is coherent noise. Coherent noise can be
199 removed by applying velocity screening in either the curvelet transform or the FK
200 transform. In this case, coherent noise removal is treated as wavefield decomposition
201 based on apparent velocity, which will be elaborated upon in the subsequent section.

202 203 *3.3 Wavefield decomposition*

204 Image processing techniques, such as the 2D Fast Fourier Transform (e.g., FK
205 transform in DAS data processing) and FDCT, have been widely used in the
206 decomposition of 2D DAS wavefields, such as the separation of seismic signals and
207 traffic noise and the separation of direct seismic waves and locally scattered seismic
208 waves (Atterholt, Zhan, Shen, et al., 2022; Williams et al., 2022). DASPy integrates the
209 FK filtering and curvelet windowing techniques in the decomposition module.

210
211 Each point within the FK domain corresponds to a specific apparent velocity. In
212 wavefield decomposition, the FK filter method employs a velocity threshold for

separation, followed by an inverse transform to produce low-speed and high-speed waveforms. Analogously, the curvelet basis utilized by the curvelet transform are wedges on the FK domain, with specific velocity ranges. The curvelet window technique separates the curvelet coefficients of the curvelet basis with different velocities. Therefore, the effects of these two techniques are nearly identical, which can be clearly determined in the FK domain of the separated waveforms. Both wavefield decomposition techniques are evaluated on stripping traffic noise from seismic waveform from the Ridgecrest DAS array (Z. Li et al., 2021; Fig. 2d). The results show that both techniques effectively enhance the signal-to-noise ratio without significant difference (Fig. 6).

3.4 Conversion to ground motions

DAS measures strain or strain rate, in contrast to ground-motion velocity and displacement used in typical seismology studies. Strain and strain rate can be converted to particle velocity and acceleration by multiplying apparent phase velocity. The difficulty of such conversion lies in the accurate estimation of apparent phase velocity of every wiggle. DASP integrates three methodologies for converting strain/strain rate into ground-motion velocity: FK rescaling (Lindsey, Rademacher, et al., 2020), curvelet transform (Yang, Atterholt, et al., 2022), and time-domain slowness determination (Lior et al., 2021). The FK rescaling method is implemented by multiplying each point in the FK domain by its corresponding apparent velocity (slope in the FK domain). Similarly,

the basis functions of the curvelet transform, which are defined in the FK domain, also correspond to varying velocity ranges. The curvelet transform conversion method multiplies each curvelet coefficient by the median velocity of its basis function. The coefficients of the largest scale basis functions, which represents waves with all velocity ($-\infty$ to $+\infty$), is set to zero. The time-domain slowness determination method obtains the apparent velocity at each time step by searching for the maximal semblance.

These three methods are tested using an M_L 4.3 earthquake recorded by a co-located DAS and seismometer array in the Brady Hot Springs (University of Wisconsin, 2016b; University of Wisconsin, 2016c; <https://gdr.openet.org/submissions/848>; <https://gdr.openet.org/submissions/846>; Fig. 3c), following H. F. Wang et al. (2018). We define a nodal geophone and a DAS channel whose distance is less than 5 m as a geophone-channel pair. Among 238 geophones and 8,621 DAS channels, we match a total of 344 geophone-channel pairs. For each geophone-channel pair, we find the corresponding linear DAS segment (Fig. 2c) and rotate the three-component geophone recording to the axial fiber direction. The original DAS strain rate recordings are integrated to strain in the time domain, and converted to velocity using FK rescaling, curvelet transform and time-domain slowness determination methods respectively (Fig. 7). We correct the DAS data timing (-1.048 s) using the GPS timing of nodal seismometers, and cross-correlate the waveforms of each geophone-channel pair with time shift less than ± 0.01 seconds. All waveforms are bandpass filtered to 1-5 Hz.

255

256 We evaluate the cross-correlation coefficient between the converted DAS velocity and
257 the rotated geophone velocity. For all 344 geophone-channel pairs, 104, 71 and 0 pairs
258 obtain cross-correlation coefficients greater than 0.7 after FK rescaling, curvelet
259 transformation and time-domain slowness determination, respectively. For this
260 particular case, the curvelet transform and the time-domain slowness determination
261 have limitations. Most linear segments consist of about 100 channels, which is not quite
262 enough for curvelet transform at larger scales. The largest scale curvelet coefficients,
263 which are set to zero, miss more details, resulting in smaller amplitudes of the converted
264 waveforms (Fig. 7). As for time-domain slowness determination methods, the
265 assumption of monochromatic wavefields makes it difficult to recover the complex
266 shallow surface scattered waves and earthquake coda waves.

267

268 **4 Discussion and Conclusions**

269 DASPpy aims to offer a user-friendly, integrated Python toolkit that facilitates the
270 analysis and processing of DAS data. Overall, the toolkit includes "basic tools" of
271 preprocessing, filtering, spectrum analysis, and visualization techniques and "advanced
272 tools" of channel attribute analysis, noise removal, wavefield decomposition, and
273 strain-velocity conversion.

274

DASPy can read and write a variety of DAS file formats, including .h5, .seggy/.sgy, .tdms and .pkl (used for storing `daspy.Section` instances). These formats are often required by other open-source software. For example, PhaseNet-DAS (W. Zhu et al., 2023) take input in .h5 or .seggy format. DASPy also supports reading DAS-RCN format as a `daspy.Section` instance which inherits the attributes from source DAS-RCN files (Lai et al., 2024). One may note that DASCORE supports more reading formats than DASPy. Also, ObsPy provides IO support for almost all traditional seismological formats, such as SAC and MiniSEED. Therefore, we provide methods (`Section.to_obs_py_stream`, `Section.to_dascore_patch`, `Section.from_obs_py_stream`, and `Section.from_dascore_patch`) for mutual transformation between `daspy.Section` instances and ObsPy's `Stream` instances (Beyreuther et al., 2010) and DASCORE's `Patch` instances (Chambers et al., 2024). These conversion functions allow smooth data flow between ObsPy, DASCORE and DASPy.

DASPy operates in the form of functions, which are designed to accommodate as many optional parameters as possible, and with sensible default values. All functions within DASPy are implemented as methods of the `daspy.Section` class. This approach is advantageous in that data attributes are stored within the class and avoid the need for manual entry. Calling functions and using methods of `daspy.Section` class are functionally equivalent, providing flexibility to suit users' needs.

296

297 Moreover, DASPy is currently programmed in pure Python for ease of use and
298 modification but in some cases computational efficiency is compromised. Consequently,
299 processing continuous data with a large number of channels and/or a high sampling rate
300 could take a long time. As an example, downsampling a 30-second waveform recorded
301 at 1000 Hz by a 10,000-channel DAS array takes 12.08 seconds. Therefore, we suggest
302 that users consider implementing CPU parallelization when undertaking large tasks.
303 Future development of DASPy could include exploring the potential of shared libraries
304 to replace computationally intensive functions.

305

306 With aforementioned designs, DASPy can be easily incorporated into the data up- and
307 down-stream tasks. The following is an example code snippet that combines DASPy
308 and ObsPy (Beyreuther et al., 2010), for a typical task phase picking in earthquake
309 monitoring:

```
>>> from daspy import read
>>> from obspy.signal.trigger import classic_sta_lta, trigger_onset
>>>
>>> sec = (
>>>     read('raw_data.h5')
>>>     .spike_removal()
>>>     .downsampling(xint=10, tint=10)
>>>     .fk_filter(fmin=1, fmax=15, vmin=2000)
>>> )
>>> sec.plot()
>>> sec.save('preprocessed_data.h5')
>>> onsets = []
>>> for d in sec.data:
>>>     cft = classic_sta_lta(d, nsta=int(0.5*sec.fs), nlta=int(5*sec.fs))
>>>     onsets.append(trigger_onset(cft, thres1=5, thres2=4))
```

310

The code reads in DAS data into an instance of `daspy.Section`, removes spike noise, performs a tenfold downsampling in both distance dimension (stacking every 10 channels into one) and time dimension (after an automatic lowpass filter), separates signal with frequency of 1-15Hz and apparent velocity less than 2000 m/s using FK filter. Subsequently, the preprocessed data is visualized, saved and fed into ObsPy to compute the short-term average/long-term average (STA/LTA; Allen & Rex, 1982) and to generate triggered picks.

As shown in the previous example, we envision that users can take advantage of DASPy to develop advanced packages developing new functions and/or modules (such as earthquake monitoring, ambient noise imaging, and traffic detection algorithms). We welcome users to contribute to the improvement and expansion of the DASPy project. Also, to foster a community of compatible packages, we add instructions for potential developers about how to contribute to the DASPy platform (<https://github.com/HMZ-03/DASPy/blob/main/CONTRIBUTING.md>). Developers are recommended to fork the DASPy repository on Github (<https://github.com/HMZ-03/DASPy/>) and submit their modifications and additions through pull requests.

Data and Resources

The RAPID dataset is openly available at <http://piweb.ooirsn.uw.edu/das/>. The traffic signals recorded by the Ridgecrest DAS can be downloaded from

<https://data.caltech.edu/records/31emd-wmv98>. The Stanford DAS-1 dataset from PubDAS is accessible via the link https://app.globus.org/file-manager?origin_id=706e304c-5def-11ec-9b5c-f9dfb1abb183&origin_path=%2F. The earthquake waveforms recorded by Brady's Geothermal Field DAS and seismometer array are available at <https://gdr.openei.org/submissions/848> and <https://gdr.openei.org/submissions/846>. The DASPpy python package is open source and available at <https://github.com/HMZ-03/DASPpy/>. We include tutorials in both English and Chinese (<https://daspy-tutorial.readthedocs.io/en/latest/>, <https://daspy-tutorial-cn.readthedocs.io/zh-cn/latest/>) and a Jupyter notebook for quick use (<https://github.com/HMZ-03/DASPpy/blob/main/document/example.ipynb>). All websites were last accessed in June 2024.

Acknowledgements

This research was supported by the National Key R&D Program of China (No. 2022YFC3005602).

Declaration of Competing Interests

The authors acknowledge there are no conflicts of interest recorded.

References

- Ajo-Franklin, J. B., Dou, S., Lindsey, N. J., Monga, I., Tracy, C., Robertson, M., et al. (2019). Distributed Acoustic Sensing Using Dark Fiber for Near-Surface Characterization and Broadband Seismic Event Detection. *Scientific Reports*, 9(1), 1–14. <https://doi.org/10.1038/s41598-018-36675-8>
- Allen, & Rex. (1982). Automatic Phase Pickers: Their Present Use and Future Prospects. *Bulletin of the Seismological Society of America*, (6), 225–242.
- Atterholt, J. (2021). Earthquake Waveforms from Curvelet-denoising Paper (Data Supplement) (1.0) [Data set]. CaltechDATA. <https://doi.org/10.22002/D1.1955>
- Atterholt, J., Zhan, Z., Shen, Z., & Li, Z. (2022). A unified wavefield-partitioning approach for distributed acoustic sensing. *Geophysical Journal International*, 228(2), 1410–1418. <https://doi.org/10.1093/gji/ggab407>
- Atterholt, J., Zhan, Z., & Yang, Y. (2022). Fault zone imaging with distributed acoustic sensing: body-to-surface wave scattering. *Journal of Geophysical Research: Solid Earth*, 127(6), 1–17. <https://doi.org/10.1029/2022jb024329>
- Bakku, S. K. (2015). Fracture Characterization from Seismic Measurements in a Borehole. *PhD Thesis*.
- Beyreuther, M., Barsch, R., Krischer, L., Megies, T., Behr, Y., & Wassermann, J. (2010). ObsPy: A python toolbox for seismology. *Seismological Research Letters*, 81(3), 530–533. <https://doi.org/10.1785/gssrl.81.3.530>

371 Biondi, B., Martin, E., Cole, S., Karrenbach, M., & Lindsey, N. (2017). Earthquakes
 372 analysis using data recorded by the Stanford DAS array. In *SEG Technical*
 373 *Program Expanded Abstracts 2017* (pp. 2752–2756).
 374 <https://doi.org/10.1190/segam2017-17745041.1>

375 Bouffaut, L., Taweesintananon, K., Kriesell, H. J., Rørstadbotnen, R. A., Potter, J. R.,
 376 Landrø, M., et al. (2022). Eavesdropping at the Speed of Light: Distributed
 377 Acoustic Sensing of Baleen Whales in the Arctic. *Frontiers in Marine Science*,
 378 9(July), 1–13. <https://doi.org/10.3389/fmars.2022.901348>

379 Brady’s Geothermal Field DAS and DTS Surface and Borehole Array Metadata [Data
 380 set]. (2016). University of Wisconsin. <https://doi.org/10.15121/1261907>

381 Brady’s Geothermal Field DAS Earthquake Data [Data set]. (2016). University of
 382 Wisconsin. <https://doi.org/10.15121/1334285>

383 Brady’s Geothermal Field Nodal Seismometer Earthquake Data [Data set]. (2016).
 384 University of Wisconsin. <https://doi.org/10.15121/1334284>

385 Candès, E., Demanet, L., Donoho, D., & Ying, L. (2006). Fast discrete curvelet
 386 transforms. *Multiscale Modeling and Simulation*, 5(3), 861–899.
 387 <https://doi.org/10.1137/05064182X>

388 Candès, E. J., & Donoho, D. L. (2004). New tight frames of curvelets and optimal
 389 representations of objects with piecewise C2 singularities. *Communications on*
 390 *Pure and Applied Mathematics*, 57(2), 0219–0266.
 391 <https://doi.org/10.1002/cpa.10116>

392 Chambers, D., Jin, G., Tourei, A., Hafiz Saeed Issah, A., Lellouch, A., Martin, E. R.,
 393 et al. (2024). DASCore: a Python Library for Distributed Fiber Optic Sensing.
 394 Chen, X. (2023). Source parameter analysis using distributed acoustic sensing – an
 395 example with the PoroTomo array. *Geophysical Journal International*, 2207–
 396 2213.
 397 Cheng, F., Chi, B., Lindsey, N. J., Dawe, T. C., & Ajo-Franklin, J. B. (2021).
 398 Utilizing distributed acoustic sensing and ocean bottom fiber optic cables for
 399 submarine structural characterization. *Scientific Reports*, 11(1), 1–14.
 400 <https://doi.org/10.1038/s41598-021-84845-y>
 401 Cohen, J. K., & Stockwell, J. W. (2008). CWP/SU: Seismic Un*x: an open source
 402 software package for seismic research and processing. *Center for Wave*
 403 *Phenomena, Colorado School of Mines*, 40.
 404 Costa, L., Martins, H. F., Martín-López, S., Fernández-Ruiz, M. R., & González-
 405 Herráez, M. (2019). Fully Distributed Optical Fiber Strain Sensor With 10–12
 406 $\epsilon/\sqrt{\text{Hz}}$ Sensitivity. *Journal of Lightwave Technology*, 37(18), 4487–4495.
 407 <https://doi.org/10.1109/JLT.2019.2904560>
 408 Dou, S., Lindsey, N., Wagner, A. M., Daley, T. M., Freifeld, B., Robertson, M., et al.
 409 (2017). Distributed Acoustic Sensing for Seismic Monitoring of the Near
 410 Surface: A Traffic-Noise Interferometry Case Study. *Scientific Reports*, 7(1), 1–
 411 12. <https://doi.org/10.1038/s41598-017-11986-4>

412 Hong, H., Wang, B., Lu, G., Li, X., Ge, Q., Xie, A., et al. (2024). Tracking Lightning
 413 Through 3D Thunder Source Location With Distributed Acoustic Sensing.
 414 *Journal of Geophysical Research: Atmospheres*, 129(4), 1–13.
 415 <https://doi.org/10.1029/2023JD038882>

416 Hudson, T. S., Baird, A. F., Kendall, J. M., Kufner, S. K., Brisbourne, A. M., Smith,
 417 A. M., et al. (2021). Distributed Acoustic Sensing (DAS) for Natural
 418 Microseismicity Studies: A Case Study From Antarctica. *Journal of Geophysical*
 419 *Research: Solid Earth*, 126(7), 1–19. <https://doi.org/10.1029/2020JB021493>

420 Jousset, P., Currenti, G., Schwarz, B., Chalari, A., Tilmann, F., Reinsch, T., et al.
 421 (2018). Dynamic strain determination using fibre-optic cables allows imaging of
 422 seismological and structural features. *Nature Communications*, 13(1).
 423 <https://doi.org/10.1038/s41467-022-29184-w>

424 Jousset, P., Currenti, G., Schwarz, B., Chalari, A., Tilmann, F., Zuccarello, L., et al.
 425 (2022). Fibre optic distributed acoustic sensing of volcanic events. *Nature*
 426 *Communications*. <https://doi.org/10.1038/s41467-022-29184-w>

427 Lai, V. H., Hodgkinson, K. M., Porritt, R. W., & Mellors, R. (2024). Toward a
 428 Metadata Standard for Distributed Acoustic Sensing (DAS) Data Collection.
 429 *Seismological Research Letters*, 95(3), 1986–1999.
 430 <https://doi.org/10.1785/0220230325>

431 Landrø, M., Bouffaut, L., Kriesell, H. J., Potter, J. R., Rørstadbotnen, R. A.,
 432 Taweessintananon, K., et al. (2022). Sensing whales, storms, ships and

433 earthquakes using an Arctic fibre optic cable. *Scientific Reports*, 12(1), 1–10.

434 <https://doi.org/10.1038/s41598-022-23606-x>

435 Li, J., Zhu, W., Biondi, E., & Zhan, Z. (2023). Earthquake focal mechanisms with

436 distributed acoustic sensing. *Nature Communications*, 14(1), 4181.

437 <https://doi.org/10.1038/s41467-023-39639-3>

438 Li, J., Kim, T., Lapusta, N., Biondi, E., & Zhan, Z. (2023). The break of earthquake

439 asperities imaged by distributed acoustic sensing. *Nature*, 620(October 2022).

440 <https://doi.org/10.1038/s41586-023-06227-w>

441 Li, Z. (2021). Recent advances in earthquake monitoring i: Ongoing revolution of

442 seismic instrumentation. *Earthquake Science*, 34(2), 177–188.

443 <https://doi.org/10.29382/eqs-2021-0011>

444 Li, Z., & Zhan, Z. (2018). Pushing the limit of earthquake detection with distributed

445 acoustic sensing and template matching: A case study at the Brady geothermal

446 field. *Geophysical Journal International*, 215(3), 1583–1593.

447 <https://doi.org/10.1093/gji/ggy359>

448 Li, Z., Shen, Z., Yang, Y., Williams, E., Wang, X., & Zhan, Z. (2021). Rapid

449 Response to the 2019 Ridgecrest Earthquake With Distributed Acoustic Sensing.

450 *AGU Advances*, 2(2). <https://doi.org/10.1029/2021av000395>

451 Lin, J., Fang, S., He, R., Tang, Q., Qu, F., Wang, B., & Xu, W. (2024). Monitoring

452 ocean currents during the passage of Typhoon Muifa using optical-fiber

distributed acoustic sensing. *Nature Communications*, 15(1).

<https://doi.org/10.1038/s41467-024-45412-x>

Lindsey, N. J., & Martin, E. R. (2021). Fiber-Optic Seismology. *Annual Review of Earth and Planetary Sciences*, 309–338.

Lindsey, N. J., Craig Dawe, T., & Ajo-Franklin, J. B. (2019). Illuminating seafloor faults and ocean dynamics with dark fiber distributed acoustic sensing. *Science*, 366(6469), 1103–1107. <https://doi.org/10.1126/science.aay5881>

Lindsey, N. J., Yuan, S., Lellouch, A., Gualtieri, L., Lecocq, T., & Biondi, B. (2020). City-Scale Dark Fiber DAS Measurements of Infrastructure Use During the COVID-19 Pandemic. *Geophysical Research Letters*, 47(16), 1–8.

<https://doi.org/10.1029/2020GL089931>

Lindsey, N. J., Rademacher, H., & Ajo-Franklin, J. B. (2020). On the Broadband Instrument Response of Fiber-Optic DAS Arrays. *Journal of Geophysical Research: Solid Earth*, 125(2), 1–16. <https://doi.org/10.1029/2019JB018145>

Lior, I., Sladen, A., Mercerat, D., Ampuero, J. P., Rivet, D., & Sambolian, S. (2021). Strain to ground motion conversion of distributed acoustic sensing data for earthquake magnitude and stress drop determination. *Solid Earth*, 12(6), 1421–1442. <https://doi.org/10.5194/se-12-1421-2021>

Luo, B., Trainor-Guitton, W., Bozdag, E., LaFlame, L., Cole, S., & Karrenbach, M. (2021). Horizontally orthogonal distributed acoustic sensing array for earthquake- And ambient-noise-based multichannel analysis of surface waves.

474 *Geophysical Journal International*, 222(3), 2147–2161.

475 <https://doi.org/10.1093/GJI/GGAA293>

476 Martin, E., Castillo, C., Cole, S., Sawasdee, P., Yuan, S., Clapp, R., et al. (2017).

477 Seismic monitoring leveraging existing telecom infrastructure at the SDASA:

478 Active, passive, and ambient-noise analysis. *The Leading Edge*, 36, 1025–1031.

479 <https://doi.org/10.1190/tle36121025.1>

480 Nayak, A., & Ajo-Franklin, J. (2021). Measurement of surface-wave phase-velocity

481 dispersion on mixed inertial seismometer – distributed acoustic sensing seismic

482 noise cross-correlations. *Bulletin of the Seismological Society of America*,

483 111(6), 3432–3450. <https://doi.org/10.1785/0120210028>

484 Nayak, A., Ajo-Franklin, J., & Team, the I. V. D. F. (2021). Distributed Acoustic

485 Sensing Using Dark Fiber for Array Detection of Regional Earthquakes.

486 *Seismological Research Letters*, 92(4), 2441–2452.

487 <https://doi.org/10.1785/0220200416>

488 Nishimura, T., Emoto, K., Nakahara, H., Miura, S., Yamamoto, M., Sugimura, S., et

489 al. (2021). Source location of volcanic earthquakes and subsurface

490 characterization using fiber-optic cable and distributed acoustic sensing system.

491 *Scientific Reports*, 11(1), 1–12. <https://doi.org/10.1038/s41598-021-85621-8>

492 Piana Agostinetti, N., Villa, A., & Saccorotti, G. (2022). Distributed acoustic sensing

493 as a tool for subsurface mapping and seismic event monitoring: A proof of

494 concept. *Solid Earth*, 13(2), 449–468. <https://doi.org/10.5194/se-13-449-2022>

495 Rørstadbotnen, R. A., Eidsvik, J., Bouffaut, L., Landrø, M., Potter, J.,
 496 Taweessintananon, K., et al. (2023). Simultaneous tracking of multiple whales
 497 using two fiber-optic cables in the Arctic. *Frontiers in Marine Science*,
 498 10(April), 1–15. <https://doi.org/10.3389/fmars.2023.1130898>
 499 Sladen, A., Rivet, D., Ampuero, J. P., De Barros, L., Hello, Y., Calbris, G., &
 500 Lamare, P. (2019). Distributed sensing of earthquakes and ocean-solid Earth
 501 interactions on seafloor telecom cables. *Nature Communications*, 10(1), 1–8.
 502 <https://doi.org/10.1038/s41467-019-13793-z>
 503 Walter, F., Gräff, D., Lindner, F., Paitz, P., Köpfli, M., Chmiel, M., & Fichtner, A.
 504 (2020). Distributed acoustic sensing of microseismic sources and wave
 505 propagation in glaciated terrain. *Nature Communications*, 11(1).
 506 <https://doi.org/10.1038/s41467-020-15824-6>
 507 Wang, H. F., Zeng, X., Miller, D. E., Fratta, D., Feigl, K. L., Thurber, C. H., &
 508 Mellors, R. J. (2018). Ground motion response to an ML 4.3 earthquake using
 509 co-located distributed acoustic sensing and seismometer arrays. *Geophysical*
 510 *Journal International*, 213(3), 2020–2036. <https://doi.org/10.1093/GJI/GGY102>
 511 Wang, X., Zhan, Z., Williams, E. F., Herráez, M. G., Martins, H. F., & Karrenbach,
 512 M. (2021). Ground vibrations recorded by fiber-optic cables reveal traffic
 513 response to COVID-19 lockdown measures in Pasadena, California.
 514 *Communications Earth & Environment*, 2(1), 1–9.
 515 <https://doi.org/10.1038/s43247-021-00234-3>

516 Wilcock, W. S. D., & Ocean Observatories Initiative. (2023). Rapid: A Community
 517 Test of Distributed Acoustic Sensing on the Ocean Observatories Initiative
 518 Regional Cabled Array [Data set]. Ocean Observatories Initiative.
 519 <https://doi.org/doi.org/10.58046/5J60-FJ89>
 520 Wilcock, W. S. D., Abadi, S., & Lipovsky, B. P. (2023). Distributed acoustic sensing
 521 recordings of low-frequency whale calls and ship noise offshore Central Oregon.
 522 *JASA Express Letters*, 3(2), 026002. <https://doi.org/10.1121/10.0017104>
 523 Williams, E. F., Fernández-Ruiz, M. R., Magalhaes, R., Vanthillo, R., Zhan, Z.,
 524 González-Herráez, M., & Martins, H. F. (2019). Distributed sensing of
 525 microseisms and teleseisms with submarine dark fibers. *Nature Communications*,
 526 10(1), 1–11. <https://doi.org/10.1038/s41467-019-13262-7>
 527 Williams, E. F., Zhan, Z., Martins, H. F., Fernández-Ruiz, M. R., Martín-López, S.,
 528 González-Herráez, M., & Callies, J. (2022). Surface Gravity Wave
 529 Interferometry and Ocean Current Monitoring With Ocean-Bottom DAS.
 530 *Journal of Geophysical Research: Oceans*, 127(5), 1–27.
 531 <https://doi.org/10.1029/2021JC018375>
 532 Xiao, H., Gaite, B., & Ruiz-barajas, S. (2022). Locating the precise sources of high-
 533 frequency microseisms using distributed acoustic sensing. *Geophysical Research*
 534 *Letters*, 0–31. <https://doi.org/10.1029/2022GL099292>
 535 Yang, Y., Zhan, Z., Shen, Z., & Atterholt, J. (2022). Fault Zone Imaging With
 536 Distributed Acoustic Sensing: Surface-To-Surface Wave Scattering. *Journal of*

537 *Geophysical Research: Solid Earth*, 127(6).

538 <https://doi.org/10.1029/2022jb024329>

539 Yang, Y., Atterholt, J. W., Shen, Z., Muir, J. B., Williams, E. F., & Zhan, Z. (2022).

540 Sub-Kilometer Correlation Between Near-Surface Structure and Ground Motion

541 Measured With Distributed Acoustic Sensing. *Geophysical Research Letters*,

542 49(1). <https://doi.org/10.1029/2021GL096503>

543 Zeng, X., Bao, F., Thurber, C. H., Lin, R., Wang, S., Song, Z., & Han, L. (2022).

544 Turning a Telecom Fiber-Optic Cable into an Ultradense Seismic Array for

545 Rapid Postearthquake Response in an Urban Area. *Seismological Research*

546 *Letters*, 93(2 A), 853–865. <https://doi.org/10.1785/0220210183>

547 Zhan, Z. (2019). Distributed acoustic sensing turns fiber-optic cables into sensitive

548 seismic antennas. *Seismological Research Letters*, 91(1), 1–15.

549 <https://doi.org/10.1785/0220190112>

550 Zhirnov, A., Stepanov, K., Chernutsky, A., Fedorov, A., Nesterov, E., Svelto, C., et

551 al. (2019). Influence of laser frequency drift in phase-sensitive optical time-

552 domain reflectometry. *Optics and Spectroscopy*, 127.

553 <https://doi.org/10.1134/S0030400X1910031X>

554 Zhu, T., & Stensrud, D. J. (2019). Characterizing Thunder-Induced Ground Motions

555 Using Fiber-Optic Distributed Acoustic Sensing Array. *Journal of Geophysical*

556 *Research: Atmospheres*, 124(23), 12810–12823.

557 <https://doi.org/10.1029/2019JD031453>

558 Zhu, T., Shen, J., & Martin, E. R. (2021). Sensing Earth and environment dynamics
 559 by telecommunication fiber-optic sensors: An urban experiment in Pennsylvania,
 560 USA. *Solid Earth*, 12(1), 219–235. <https://doi.org/10.5194/se-12-219-2021>
 561 Zhu, W., Biondi, E., Li, J., Yin, J., Ross, Z. E., & Zhan, Z. (2023). Seismic Arrival-
 562 time Picking on Distributed Acoustic Sensing Data using Semi-supervised
 563 Learning. *Nature Communications*, 14(1), 1–17. [https://doi.org/10.1038/s41467-](https://doi.org/10.1038/s41467-023-43355-3)
 564 023-43355-3

565 **Full mailing address for each author**

566 Minzhe Hu: Laboratory of Seismology and Physics of Earth's Interior, School of Earth
 567 and Space Sciences, University of Science and Technology of China, No.96, JinZhai
 568 Road Baohe District, Hefei, Anhui, 230026, P.R.China.

569 Zefeng Li: Laboratory of Seismology and Physics of Earth's Interior, School of Earth
 570 and Space Sciences, University of Science and Technology of China, No.96, JinZhai
 571 Road Baohe District, Hefei, Anhui, 230026, P.R.China.

572

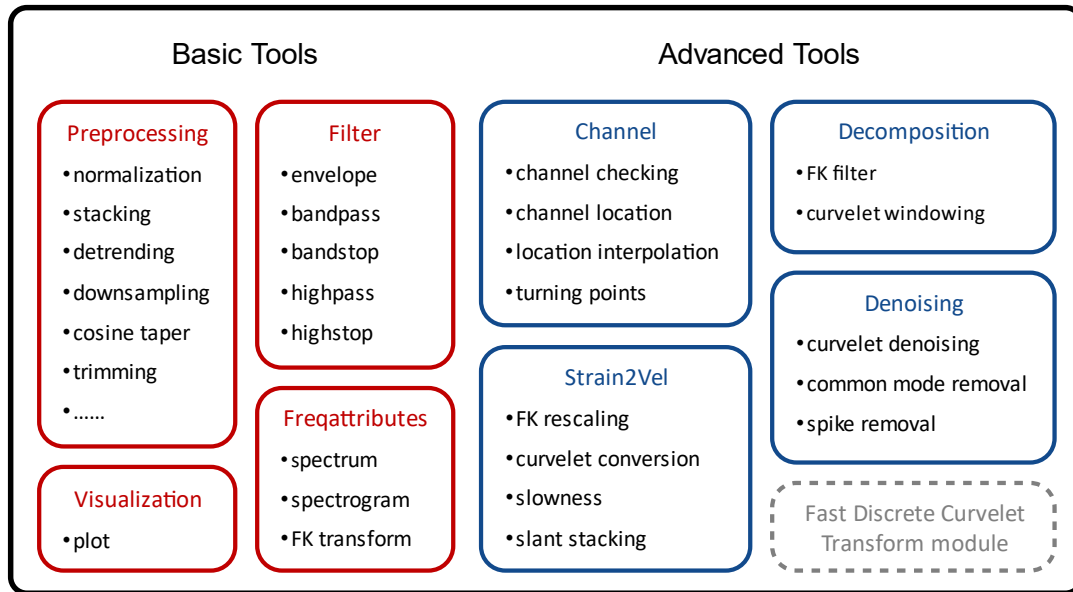
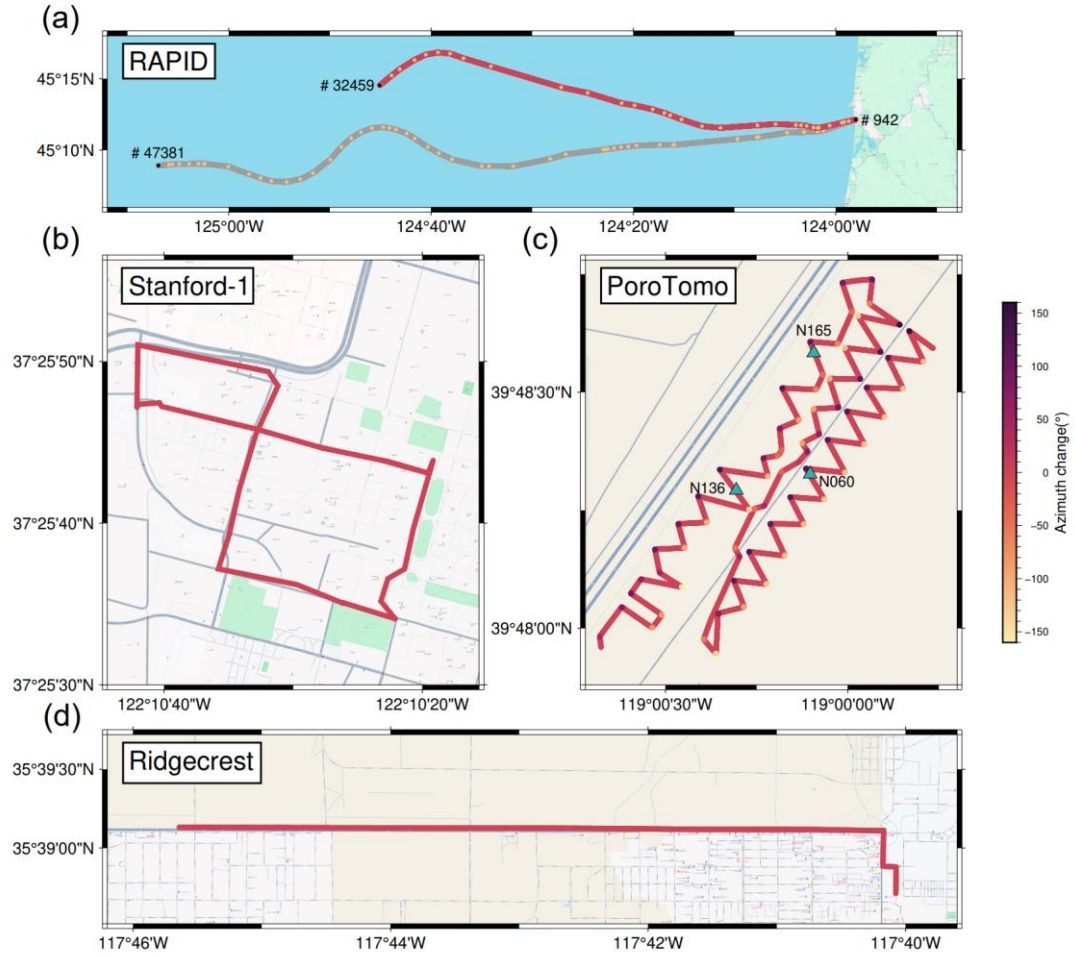


Figure 1. Main structure of DASPpy toolbox. Each block indicates a module composed of multiple user-facing functions. The modules for basic tools are shown in red boxes, and modules for advanced tools are shown in blue boxes. The module within the gray dotted box is specifically built for discrete fast curvelet transforms.



579

580 **Figure 2.** Geometry of DAS arrays whose data we used for testing. (a) RAPID DAS
 581 arrays that land at Pacific City, Oregon (Wilcock & Ocean Observatories Initiative.,
 582 2023). The red line indicates the array that we utilized for our test (referring to the north
 583 cable here), which is the same for (b) and (d). The grey line indicates the south cable,
 584 whose data are not used. The black dots represent three points along the cable with
 585 known coordinates and channel numbers, while the orange dots represent the those with
 586 known coordinates but unknown channel number. (b) Stanford campus array in
 587 California (Biondi et al., 2017; Martin et al., 2017). (c) Brady's geothermal field DAS
 588 array (University of Wisconsin, 2016b) and three co-located geophone stations

589 (University of Wisconsin, 2016c) in Nevada. The color of the DAS cable indicates the
590 azimuth change of the cable before and after the corresponding channel. (d) DAS arrays
591 started after the 2019 M_w 7.1 Ridgecrest earthquake, California (Atterholt, Zhan, Shen,
592 et al., 2022; Z. Li et al., 2021).

593

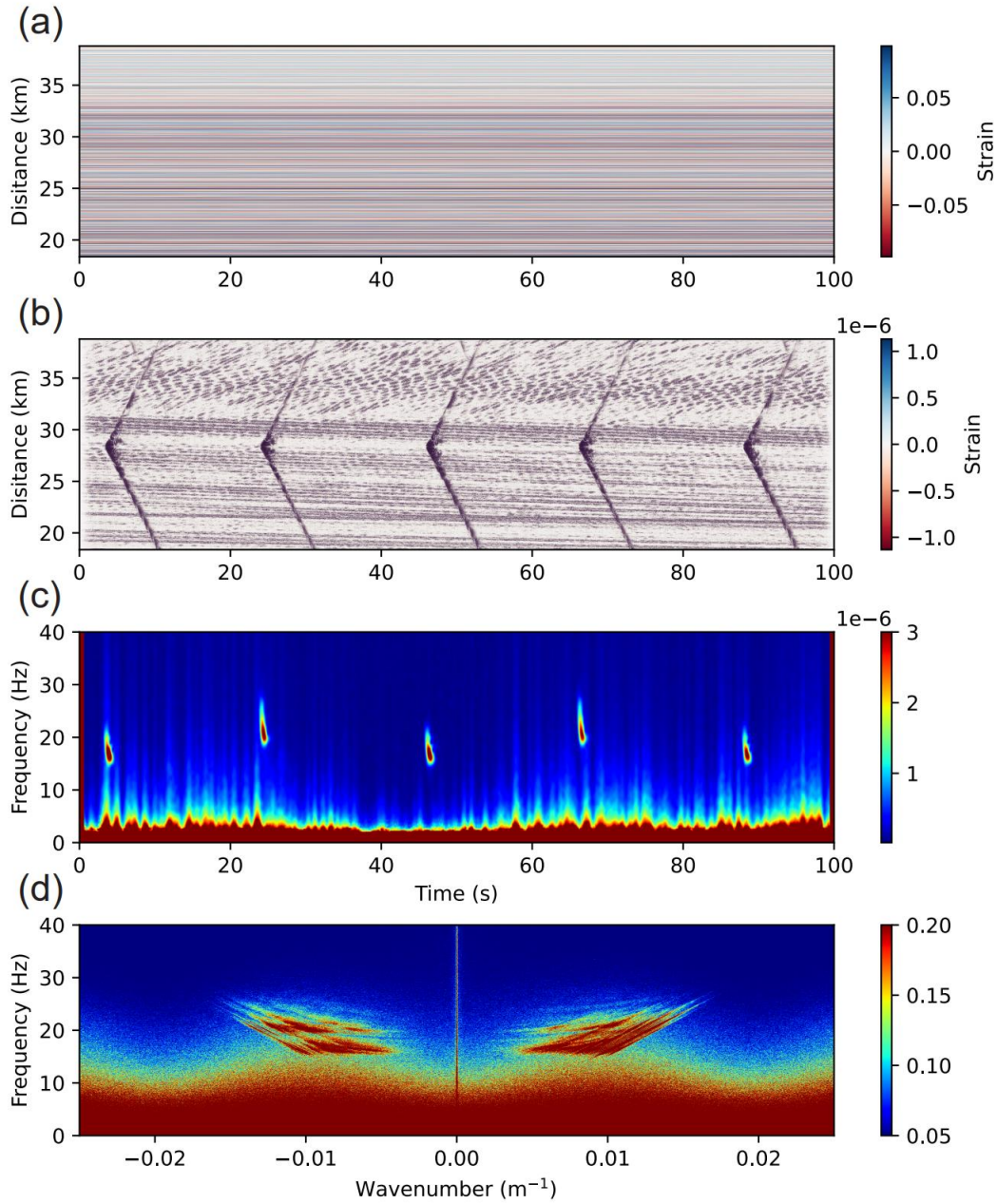


Figure 3. Demonstration of signal processing and visualization. (a) Original strain recording for 100 seconds beginning on November 4, 2021, 01:59:02 UT, recorded by the Optasense interrogator channel 9000-19000 on north ocean-bottom cable from RAPID dataset (Wilcock & Ocean Observatories Initiative., 2023). (b) Filter to 15-27 Hz, following Wilcock et al. (2023). (c) Spectrogram averaged over 100 channels. (d) FK spectrum calculated from 2D fast Fourier transform.

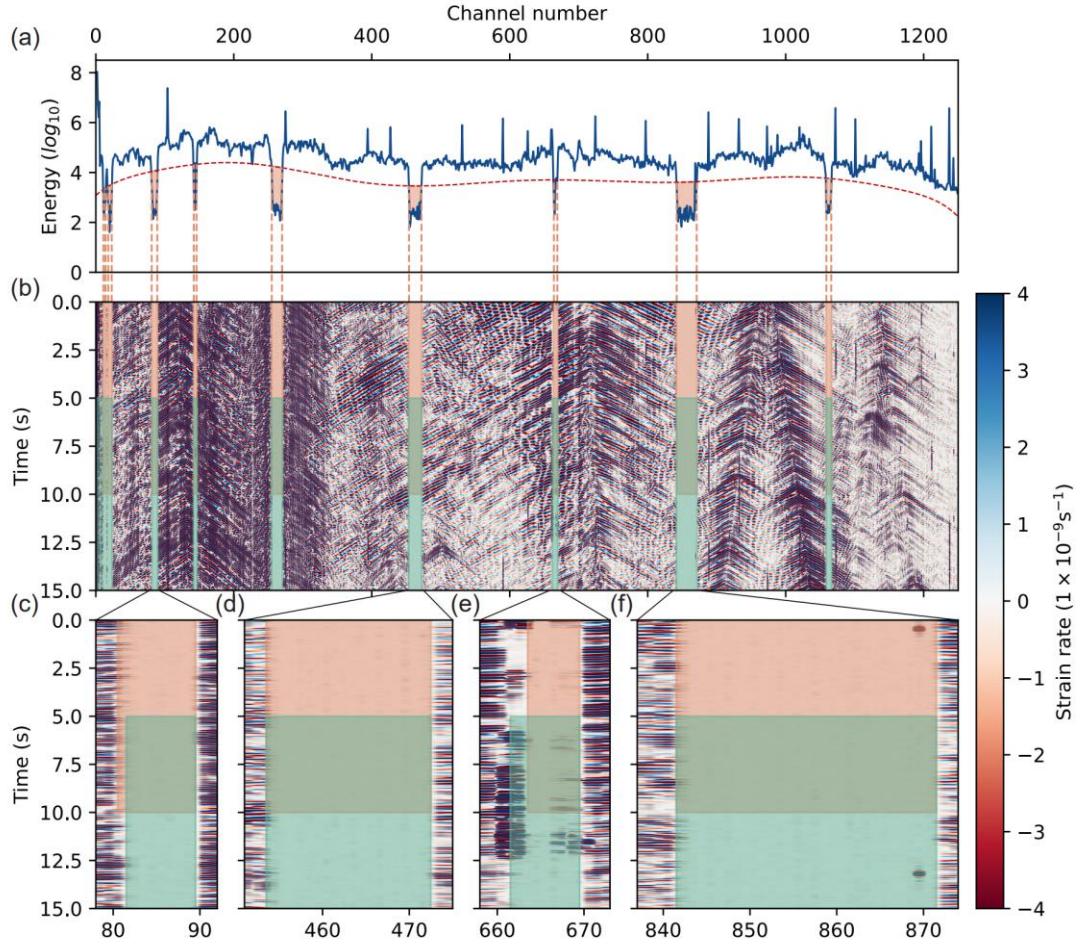


Figure 4. Bad channel detection of the DAS array near Ridgecrest, CA. (a) Energy curve (blue line) and thresholds (red dotted line) for bad channel detection. (b) DAS recording of 15-second traffic noise (Atterholt, 2021) used for bad channel detection. Orange areas indicate bad channels detected by our function, while green areas are bad channels picked by Atterholt, Zhan, Shen, et al. (2022). (c)-(f) Zoom-in plot of four parts of the DAS recording. Channel 81 (c) and channels 662&663 (e) are identified differently by our function and Atterholt, Zhan, Shen, et al. (2022).

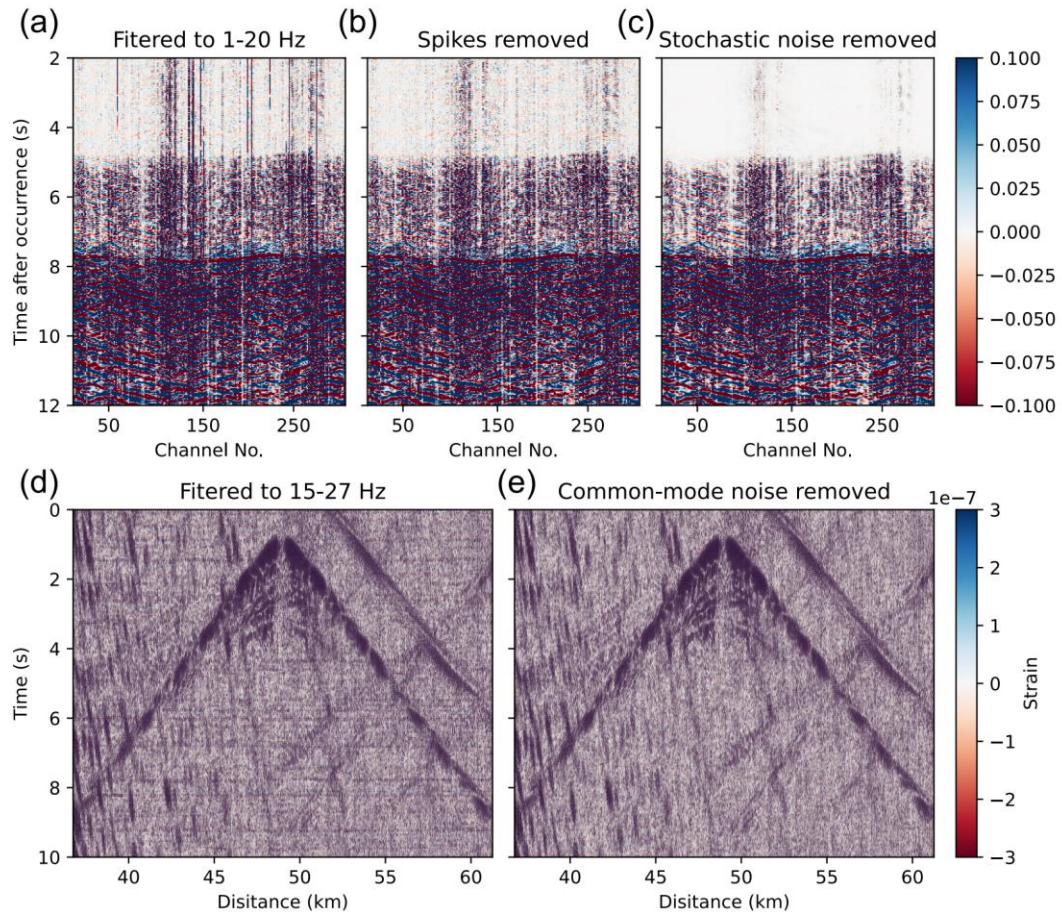


Figure 5. Cases of wavefield denoising. (a) Waveforms of an M_D 2.8 earthquake (<https://earthquake.usgs.gov/earthquakes/eventpage/nc73940346/executive>) recorded by Stanford-1 DAS array (Biondi et al., 2017; Martin et al., 2017). Bad channels are removed and bandpass filter to 1-20 Hz. (b) Waveforms with spikes removed based on (a). (c) Waveforms with stochastic noise removed by curvelet transform based on (b). (d) Strain recording filtered to 15 to 27 Hz for 10 seconds beginning on November 4, 2021, 01:59:22 UT, recorded by the Optasense interrogator on north ocean-bottom cable from RAPID dataset (Wilcock & Ocean Observatories Initiative., 2023). (e) Waveforms with common-mode noise removed based on (d).

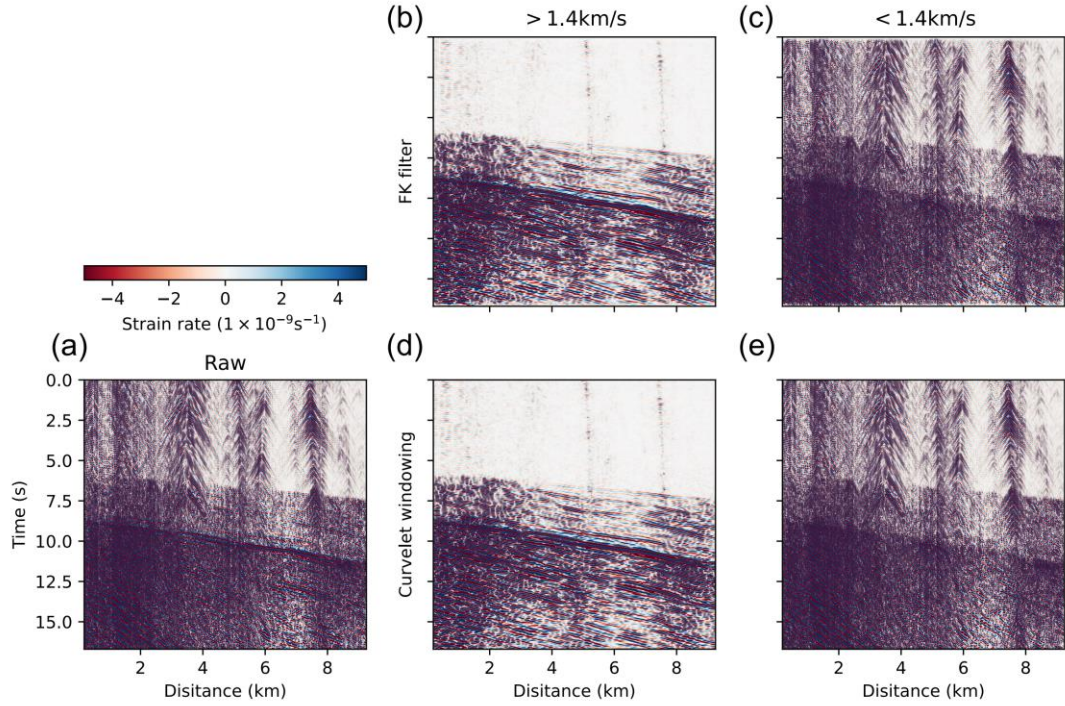


Figure 6. An example of wavefield decomposition. (a) Waveforms of an M_L 2.6 earthquake (<https://earthquake.usgs.gov/earthquakes/eventpage/ci38972328/executive>) recorded by Ridgecrest DAS array (Z. Li et al., 2021), with spikes removed. (b) Waveforms with an FK filter to retain energy with an apparent velocity $> 1.4 \text{ km/s}$ (cosine tapered from 1.2–1.6 km/s). (c) Waveforms with an FK filter to retain energy with an apparent velocity $< 1.4 \text{ km/s}$ (cosine tapered from 1.2–1.6 km/s). (d) Waveforms with curvelet windowing to retain energy with an apparent velocity $> 1.4 \text{ km/s}$. (e) Waveforms with curvelet windowing to retain energy with an apparent velocity $< 1.4 \text{ km/s}$.

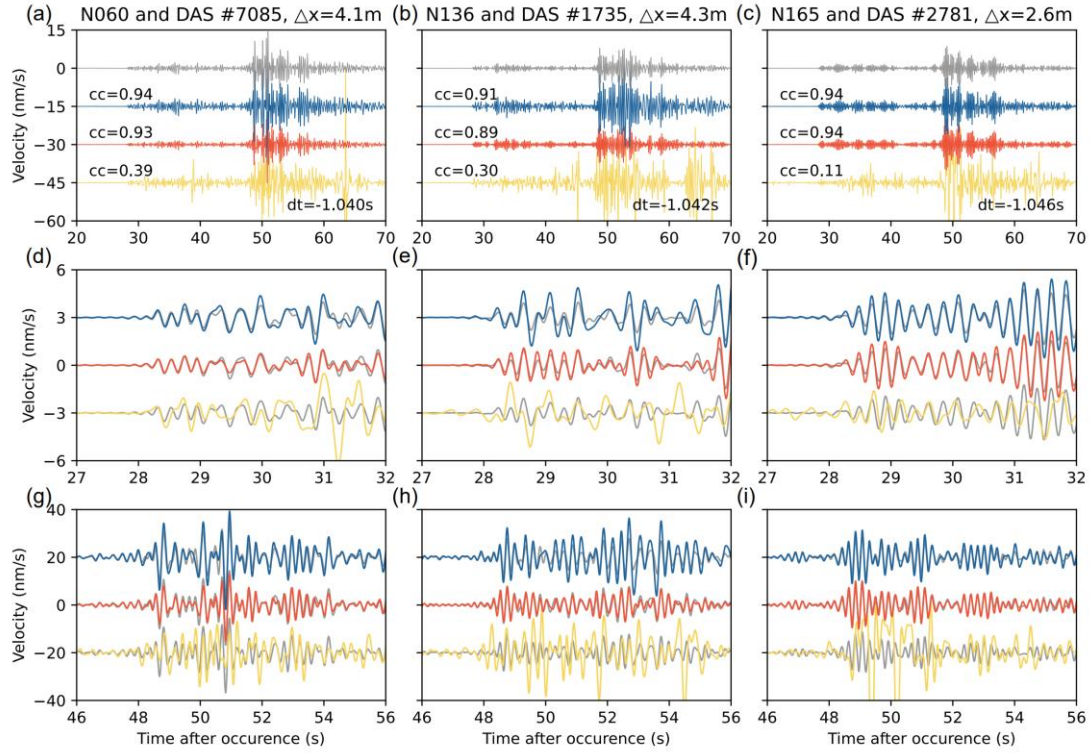


Figure 7. Conversion from strain to velocity by three methods of M_L 4.3 Hawthorne earthquake (<https://earthquake.usgs.gov/earthquakes/eventpage/nn00536374>) recorded by Brady's geothermal field DAS array. (a)-(c) Rotated geophone velocity (grey), and velocity converted from integrated DAS strain by FK-rescaling (blue), curvelet transform (red) and time-domain slowness determination (yellow), same as below. All waveforms are bandpass filtered to 1-5 Hz. (d)-(f) Zoom-in window for P arrival of (a)-(c). (g)-(i) Zoom-in window for S arrival of (a)-(c).